# CFD and experimental studies of Heavy Fuel Oil sprays for marine engine applications

P. Kontoulis*[1], L. Kaiktsis[1], B. von Rotz[2], A. Schmid[2],
G. Weisser[2], K. Herrmann[3], K. Boulouchos[4]
[1]Division of Marine Engineering,
Department of Naval Architecture and Marine Engineering,
National Technical University of Athens, Greece
[2]Wärtsilä Switzerland Ltd, CH-8401 Winterthur, Switzerland
[3]Paul Scherrer Institute, CH-5232 Villigen PSI, Switzerland
[4]Aerothermochemistry and Combustion Systems Laboratory, ETH Zürich,
CH-8092 Zürich, Switzerland
*Corresponding author: pkontoul@mail.ntua.gr

**Abstract**

A major development for experimental studies in the context of marine Diesel engines was achieved in the course of the EU funded research project HERCULES (High-Efficiency R&D on Combustion with Ultra Low Emissions for Ships). In particular, a state-of-the-art experimental test facility, dedicated to spray and combustion studies under conditions similar to those of large marine Diesel engines, was developed by Wärtsilä Switzerland and ETH Zürich. This Spray Combustion Chamber (SCC) facility enables detailed flow, spray, combustion and emission formation studies. Thus, valuable experimental data can be attained for characterizing spray and combustion, as well as for validating and supporting model development for Computational Fluid Dynamics (CFD) studies.

Heavy Fuel Oil (HFO) is the predominant fuel in the marine industry. Recently, a detailed model predicting the thermophysical properties of marine HFO of arbitrary composition was developed by the authors. The model is based on a one-component approach, and requires an input of four values of fuel properties, commonly measured at bunkering, namely: (a) density at a given temperature, (b) kinematic viscosity values at two temperatures, and (c) sulfur content. The model predicts a large set of fuel properties relevant for CFD studies, such as molecular weight, carbon-to-hydrogen ratio, enthalpy of formation, pseudo-critical pressure and temperature values, as well as the temperature dependence of density, viscosity, vapor pressure, heat of evaporation, sensible enthalpy, surface tension and mass diffusion coefficient.

In the present study, the model is utilized for extensive CFD studies of HFO spray dynamics in the SCC, and results are compared against experiments. Here, the model is utilized to predict the thermophysical properties of the HFO used in the experiments. Spray modeling is based on a proper adaptation of the Cascade Atomization and drop Break-up (CAB) model. Simulations are performed with a KIVA-3 based CFD code for non-reactive evaporating conditions; the computational results are found to accurately reproduce the experimental data for spray penetration length and cone angle. The effects of HFO preheating on spray development are demonstrated. Further, spray propagation under non-evaporating conditions is investigated, and computational results are found in good agreement with experimental data reported in literature. Finally, first experimental and computational reactive spray studies in the SCC are reported, aiming at a characterization of reactive flow in terms of ignition delay and location; a good agreement between experiments and computations is demonstrated. The present investigation builds a strong basis for further combined computational/experimental studies of non-reactive and reactive HFO sprays under conditions relevant for large marine engines.

## Introduction

Recent studies indicate that the pollutant emissions from ships are substantial. In particular, the emissions of $CO_2$, NOx and SOx correspond to 2-3%, 10-15% and 4-9%, respectively, of the global anthropogenic emissions [1]. Hence, the International Maritime Organization (IMO) and several national authorities have set strict regulations in terms of marine engine pollutant emissions, and have adopted mechanisms that ensure the efficient performance of vessels [2]. In addition, the current maritime market, affected by the global economic crisis, imposes low freight rates, while fuel price is continuously soaring. As a result, ship owners and charterers are forced to drastically reduce the ship operational costs. This involves an overall optimization of ship propulsion systems, and can be supported by lowering the vessel's speed (slow steaming) [3], [4]. Under these circumstances, the engine manufacturers, supported

by the international research community, make substantial efforts for improving the design and operation of marine engines.

The EU funded research project HERCULES (High-Efficiency R&D on Combustion with Ultra Low Emissions for Ships) constitutes a long-term research initiative, aiming at developing novel engine technologies for reducing pollutant emissions and improving efficiency and reliability of marine engines [5], [6]. In this frame, a state-of-the-art SCC experimental test facility was developed by Wärtsilä Switzerland and ETH Zürich, for spray and combustion studies under conditions similar to those of large marine engines, [7], [8]. Thus, valuable experimental evidence can be obtained and used in studying and optimizing flow and combustion in marine engines. Apart from providing a deeper insight into and a better understanding of spray development and combustion, such experiments are expected to substantially support worldwide research on large marine engines, by supporting model development and validation for CFD studies. It is noted that the majority of physical models used in engine CFD has been validated for geometries and conditions relevant for small or heavy duty engines [9]. However, the operating conditions of marine engines, especially large two-stroke marine Diesel engines, are substantially different [10], due to the following reasons:

- The injectors are located in the periphery of the cylinder cover, instead of the cylinder center.
- Two or three injectors per cylinder (instead of one) are used.
- Each injector carries multiple orifices with different spatial orientation and diameter.
- The orifice diameter is large (in the range of 1 mm).
- The injection and combustion duration are long.
- There is a strong air swirling motion, due to the requirements of scavenging.
- The fuel and lubricant quality are different (Light Fuel Oil (LFO), HFO, cylinder oil).
- Due to the low speed (less than 200 rpm) and the large dimensions, time and length scales are both increased.

It is widely accepted today that CFD studies can substantially contribute to understanding and optimizing engine aerothermochemistry, provided the key in-cylinder processes such as spray break-up, evaporation, fuel-air mixing, ignition and combustion are properly described. The effectiveness of CFD modeling depends crucially on the precision of fuel thermophysical properties utilized, which previously posed some limitations with respect to the applicability of CDF simulations to marine Diesel engine operation in view of the fact that HFO is the predominant fuel in this industry. In order to overcome those limitations, a detailed model of marine HFO thermophysical properties was recently developed by the authors [11]. In the present investigation, this model is applied to predict the properties of the specific HFO used in the experiments of Wärtsilä Switzerland and ETH Zürich [12] and used in conjunction with the CAB model for spray atomization and droplet break-up, which has proven to be a useful tool for predicting spray dynamics [13]. An extensive CFD study is performed here to simulate non-reactive and reactive HFO sprays in the SCC facility, and the computational results are validated against corresponding experimental data. The objectives of the present investigation are: (a) to further validate the HFO thermophysical properties model introduced in [11], (b) to properly adapt the CAB model for HFO spray simulations, and (c) to characterize the dynamics of non-reactive and reactive HFO sprays under conditions relevant for large marine engines.

**Experimental test facility and methods**

The SCC facility is a unique development, which enables the experimental investigation of injection and combustion processes in relation to large two-stroke marine engines, at relevant physical dimensions (bore) and operational parameters (pressure, temperature), including flow characteristics (swirl) and low quality fuels (HFO). Figure 1 gives an overview of the entire test facility (left), and schematically illustrates the setup and the operational principle of the experiments (right). The core element is a disk-shaped constant volume spray combustion chamber, with a diameter of 500 mm and a height of 150 mm. A peripheral injection into a swirling gas flow is implemented, at the chamber mid-plane. Optical access is provided by sapphire windows (net diameter of 150 mm) mounted in eccentric revolvable window holders located in rotatable covers. At the start of injection, conditions similar to those in real large marine engines can be achieved (levels up to 13 MPa, 930 K) by feeding the chamber via inclined intake channels with pressurized and heated gas provided by pressure vessels connected to a heat regenerating system [7], [8].

An improved "shadow-imaging" method consisting of a pulsed diode laser light source and an appropriate narrow band pass filter (CWL 689.1 nm, T 60%, FWHM 10.6 nm) is applied for visualizing the macroscopic spray morphology inside the spray combustion chamber [14]. A very short laser pulse within a 1μs exposure time of a high-speed CMOS-camera (20 kHz frame rate, 512x512 pixels) enables a high signal-to-noise ratio in the recordings.

For detecting the flame region in reactive cases, a high speed intensifier connected to a second high speed camera has been added to the experimental setup, in order to simultaneously record shadow images and UV light

emitted from the combustion (see [15]). An appropriately configured setup is used to investigate the ignition location and flame lift-off length. In parallel, the global broadband light signal is recorded with a photo diode, allowing the measurement of the ignition delay independently of the recording rate, with a higher sampling rate.

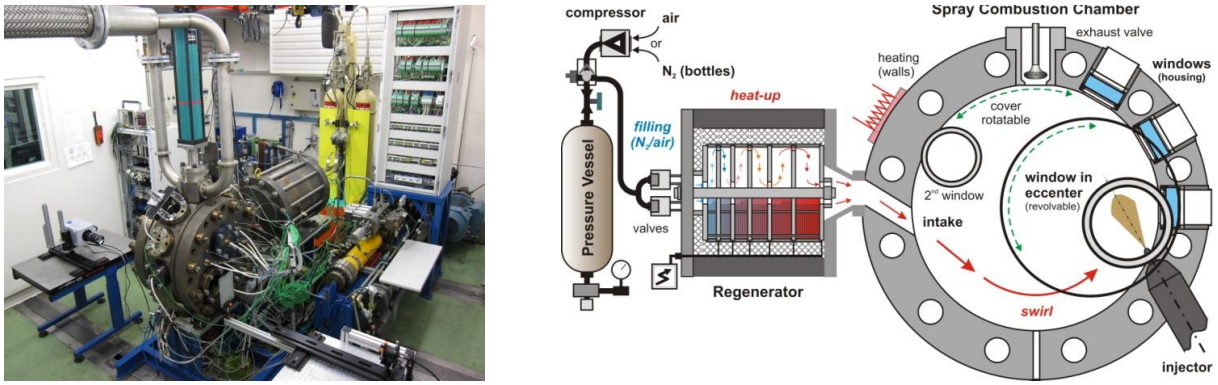


**Figure 1:** Overview (left) and schematic of the SCC facility indicating the operational principle of the experiments (right).

## CFD modeling

*CFD code*

CFD engine simulations commonly involve the numerical solution of the Reynolds averaged conservation equations for mass, momentum and energy, utilizing physical models to account for the specific phenomena of engine fluid mechanics and combustion. Such phenomena include, for instance, the breakup and evaporation of the fuel spray interacting with the turbulent multi-component gas flow. In the present work, the KIVA-3 CFD code is utilized [16], [17], with the k-ε turbulence model for turbulence modeling.

*Computational grid*

A finite volume mesh is used to discretize the domain considered in the present study, i.e. the disk-shaped constant volume SCC [7], [8]. Taking into account the large size of the chamber, grid generation has aimed at effective block-structured meshes, for adequately resolving the spray regime, while maintaining a reasonable computational cost [17]. The investigation converged to a sixty three block grid, characterized by a constant azimuthal resolution of 2.0 degrees. Figure 2 shows the front and bottom views of a grid used in the present study. In the spray regime in front of the injector, the cells are characterized by equal increments in the x (radial) and z (vertical) direction; different grid densities have been tested, characterized by cells of 4X4 mm, 2X2 mm and 1X1 mm. Information regarding the three grids utilized in detailed spatial resolution studies is reported in Table I.

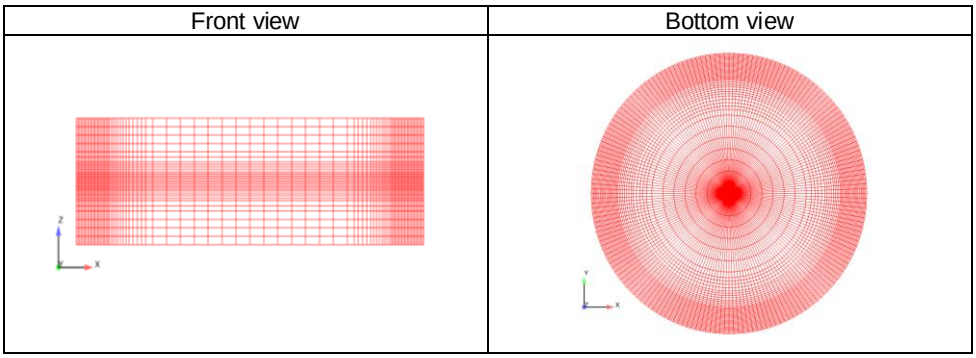


**Figure 2:** Front and bottom views of a grid used in the present SCC simulations.

**Table I:** Features of the meshes utilized in spatial resolution tests.

| Mesh (Ø500x150 mm) | Number of cells | Spray regime resolution |
|---|---|---|
| Coarse | 115,000 | 4 mm |
| Fine | 260,000 | 2 mm |
| Very fine | 720,000 | 1 mm |

*Test cases*

Both evaporating and non-evaporating non-reactive HFO sprays have been computed; the evaporating cases correspond to conditions and injection characteristics utilized in the experimental studies of [12]. Further, simulations have been performed for reactive HFO sprays, corresponding to new experiments. In the non-reactive evaporating cases, densities of the surrounding gas (nitrogen) of 11.2, 22.5 and 33.7 kg/m$^3$ have been considered, and the results have been validated against the experiments reported in [12], in terms of spray penetration length and cone angle. In the case of non-reactive non-evaporating spray, the high gas density of 33.7 kg/m$^3$ has been selected. Finally, simulations of reactive HFO sprays have been performed, for a surrounding air density of 34.5 kg/m$^3$, and the results compared against the new experiments, in terms of ignition delay and location. A swirling gas flow has been considered at the start of injection, with velocities prescribed in terms of a Bessel function, corresponding to a solid body swirl angular velocity of 100 rad/s. The cases computed are summarized in Table II, while important input data are presented in Table III.

**Table II:** Cases computed in the present study.

| Filling gas: nitrogen ($N_2$) – non-reactive flow | | | | | Filling gas: air – reactive flow |
|---|---|---|---|---|---|
| Case | 1 | 2 | 3 | 4 | 5 |
| Gas temperature [K] | 900 (evaporating) | | | 400 (non-evaporating) | 915 (evaporating) |
| Gas pressure [bar] | 90 | 60 | 30 | 40 | 91 |
| Gas density [kg/m$^3$] | 33.7 | 22.5 | 11.2 | 33.7 | 34.5 |
| Swirl angular velocity [rad/s] | 100 (Bessel function profile) | | | | |

**Table III:** Simulation input data.

| | |
|---|---|
| Injection system | Common Rail |
| Number of nozzle holes | 1 |
| Diameterof nozzle hole [mm] | 0.875 |
| Injection pressure [bar] | 1000 |
| Injector nozzle orientation | co-swirl |
| HFO preheating temperature [°C] | 120 |
| Wall temperature [K] | 453 |

*HFO thermophysical properties model*

In CFD simulations, the performance of physical models accounting for the main in-cylinder processes, i.e. fuel spray break-up, evaporation, ignition and combustion, depends critically on the accuracy of the values of fuel thermophysical properties. In the present study, a detailed model of HFO thermophysical properties, recently developed by the authors [11], is used for calculating the values and temperature dependence of the properties required in CFD modeling. The development of the present model is based on an extensive body of literature studies on heavy petroleum fractions, and considers marine HFO as an equivalent one-component heavy fraction of undefined composition; the model thus follows an approach widely adopted in literature CFD studies for distillate fuels (e.g. approximation of LFO properties with those of n-tetradecane – $C_{14}H_{30}$). The model can account for variable fuel composition; to this end, it requires an input of four values of fuel properties, commonly measured at fuel bunkering: (a) density at a given temperature, (b) kinematic viscosity values at two temperatures, and (c) sulfur content. Here, the model input data set is based on the measured values of thermophysical properties of the HFO utilized in [12], reported therein. The input data, as well as the resulting values of main properties, i.e. molecular weight, carbon-to-hydrogen atomic ratio, specific heat capacity, enthalpy of formation, Lower Heating Value (LHV) and Calculated Carbon Aromaticity Index (CCAI), characterizing the particular HFO, are reported in Table IV. The computed temperature dependence of density and kinematic viscosity is presented in Figure 3, while the corresponding dependence of dynamic viscosity and vapor pressure, including the pseudo-critical point, is shown in Figure 4. Figure 5 shows the temperature dependence of heat of evaporation and sensible enthalpy, while the corresponding curves of surface tension and mass diffusivity (fuel vapor to air) are presented in Figure 6. In all cases, data regarding the thermophysical properties of n-tetradecane – $C_{14}H_{30}$ are also included [17], [18], with the comparison indicating the

substantial difference between the values corresponding to light and heavy hydrocarbons. The computed values of HFO thermophysical properties have been imported to the fuel library of the KIVA-3 code.

**Table IV:** Measured and computed, utilizing the model reported in [11], values of thermophysical properties of the HFO used in [12]. Corresponding values for $C_{14}H_{30}$ are included for reference [17], [18].

| | Thermophysical property | HFO of [12] | $C_{14}H_{30}$ |
|---|---|---|---|
| Input data | Density at 288.15 K | 1001.1 kg/m$^3$ | 765.7 kg/m$^3$ |
| | Kinematic viscosity at 323.15 K | 1255 cSt | 1.841 cSt |
| | Kinematic viscosity at 288.15 K | 42504.5 cSt | 3.428 cSt |
| | Sulphur weight content | 0.806% | - |
| Results | Molecular weight | 554.84 gr/mole | 198.388 gr/mole |
| | Carbon-to-hydrogen atomic ratio | 0.977 | 0.467 |
| | Specific heat capacity at 298.15 K | 1.4117 KJ/kgK | 1.639 KJ/kgK |
| | Enthalpy of formation at 298.15 K | 1019 KJ/Kg | -1675.7 KJ/Kg |
| | LHV | 40826.2 KJ/Kg | 46095 KJ/Kg |
| | CCAI | 851 | - |

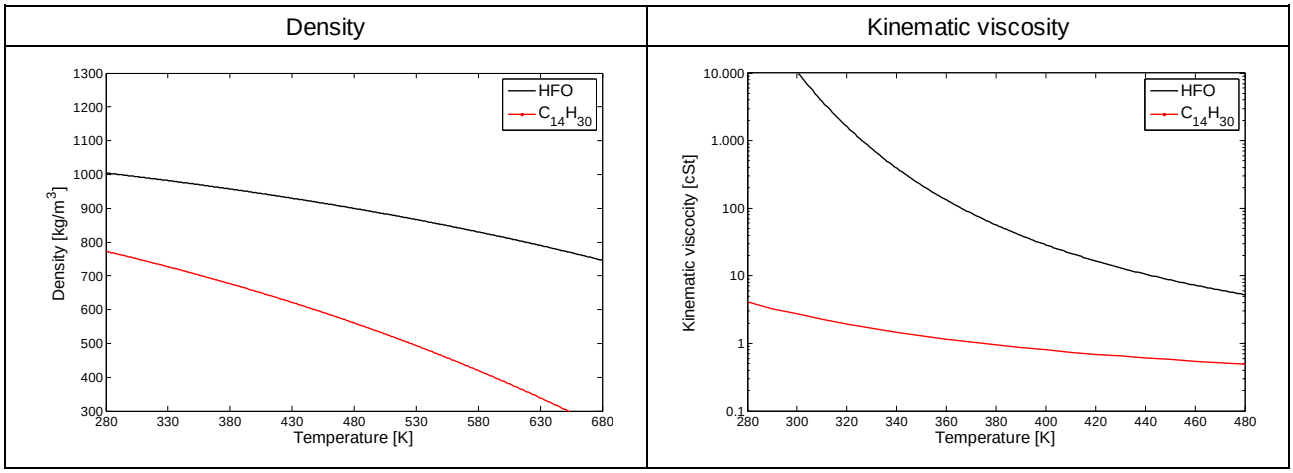


**Figure 3:** Computed temperature dependence [11] of density (left) and kinematic viscosity (right) of the HFO used in [12]. A corresponding curve for $C_{14}H_{30}$ is included for reference [17], [18].

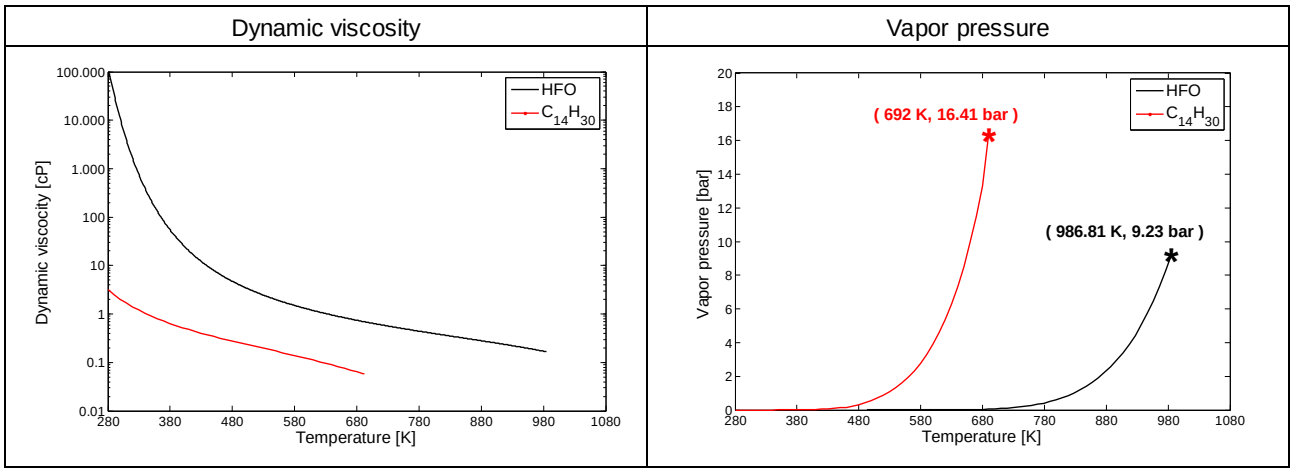


**Figure 4:** Computed temperature dependence [11] of dynamic viscosity (left) and vapor pressure, including the pseudo-critical point, (right) of the HFO used in [12]. A corresponding curve for $C_{14}H_{30}$ is included for reference [17], [18].

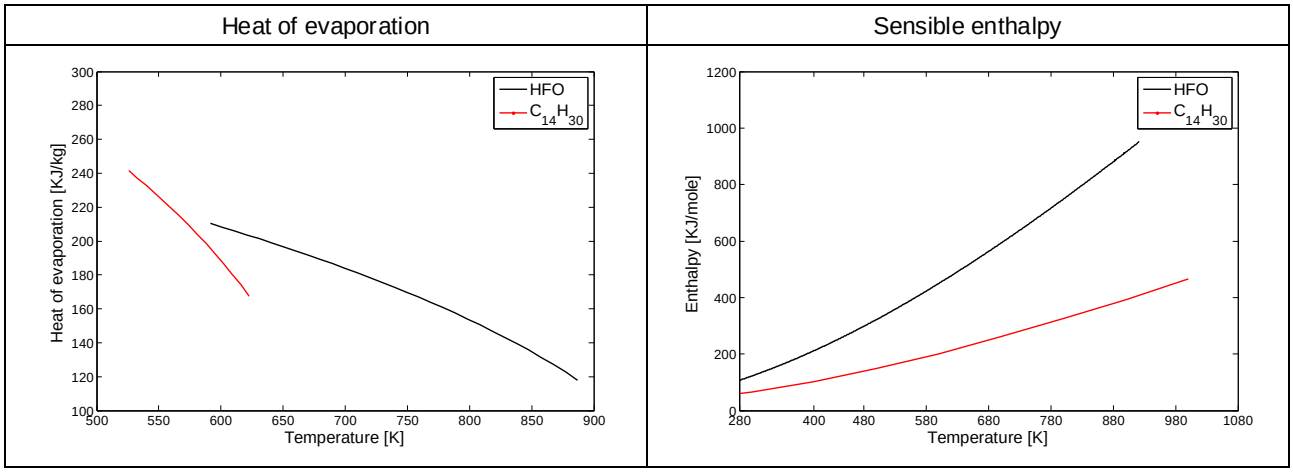


**Figure 5:** Computed temperature dependence [11] of heat of evaporation (left) and sensible enthalpy (right) of the HFO used in [12]. A corresponding curve for $C_{14}H_{30}$ is included for reference [17], [18].

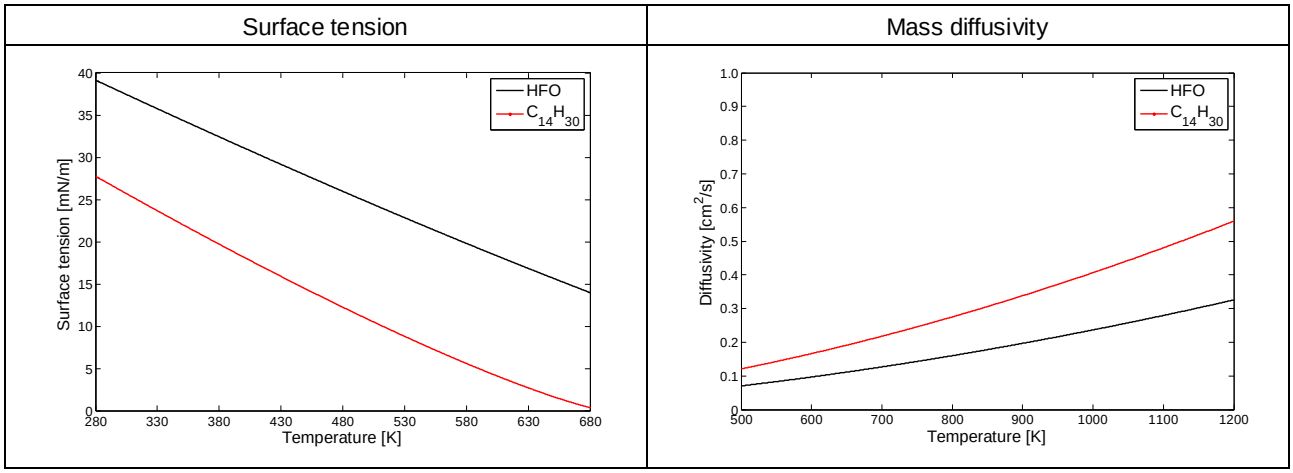


**Figure 6:** Computed temperature dependence [11] of surface tension (left) and mass diffusivity (fuel vapor to air at 1 atm) (right) of the HFO used in [12]. A corresponding curve for $C_{14}H_{30}$ is included for reference [17], [18].

*CAB spray model*

In the present simulations, modeling of the liquid fuel spray is performed on the basis of the CAB model [13], which constitutes an extension of the Enhanced Taylor Analogy Break-up (ETAB) model [19], [20]; both models are basically further developments of the Taylor Analogy Break-up (TAB) model, introduced by O' Rourke et al. [21]. The CAB model adopts the analogy between an oscillating drop penetrating into a gas (with a given relative velocity) and a forced damped spring-mass system, as in TAB and ETAB. The modifications introduced in CAB concern the Initial Droplet Size Distribution (IDSD), the initial conditions regarding the deformation velocity, and the calculation of the number and size of the product droplets, resulting from break-up. In more detail, the initially injected droplets follow a power law IDSD, accounting for droplet surface stripping close to the nozzle exit. In the present study, the IDSD introduced in [13] is implemented for the injected parcels:

$$g(r) = \frac{n+4}{r_0} \cdot \left( \frac{r}{r_0} \right)^{n+3} \tag{1}$$

where, $r$ is the droplet radius, $r_0$ is the nozzle radius and $n$ is a model constant. Further, the choice of the initial deformation velocity takes into account that the first break-up of an injected drop occurs at a certain distance from the nozzle tip, which is calculated via the following experimentally determined formula [22]:

$$L_b = U_i \cdot t_{bu} = C_\lambda \cdot d_0 \cdot \sqrt{\frac{\rho_l}{\rho_s}} \tag{2}$$

where, $U_i$ is the jet exit velocity, $t_{bu}$ is the drop break-up time, $C_\lambda$ is a model constant depending on the nozzle design, $d_0$ is the nozzle diameter, $\rho_l$ is the fuel density and $\rho_s$ is the density of the surrounding gas. Finally, the product droplet number and size is related to the break-up time via a proportionality constant, $K_{bu}$, which accounts for three regimes, namely, bag, stripping and catastrophic break-up. It is noted that $K_{bu}$ is specified through the droplet oscillation frequency, $\omega$, and the Weber number, $We$, as follows:

$$K_{bu} = \begin{cases} k_1 \cdot \omega, \ if \ We \le We_{b,s} \ (bag \ break-up) \\ k_2 \cdot \omega \cdot \sqrt{We}, \ if \ We_{b,s} < We \le We_{s,c} (stripping \ break-up) \\ k_3 \cdot \omega \cdot We^{3/4}, \ if \ We > We_{s,c} \ (catastrophic \ break-up) \end{cases} \quad (3)$$

where, $k_1$, $k_2$ and $k_3$ are model constants, $\omega$ is the droplet oscillation frequency, $We$ is the Weber number of the drop before break-up, $We_{b,s}$ is the transition Weber number between bag and stripping break-up and $We_{s,c}$ is the transition Weber number between stripping and catastrophic break-up. $We_{b,s}$ has a suggested value of 80, while the suggested value of $We_{s,c}$ is 350 [23]. In CAB, the model constants $k_1$, $k_2$ and $k_3$ are based on experimental measurements of drop size, and the transition between the individual break-up regimes, as expressed by $K_{bu}$, is considered continuous. Consequently, only the value of $k_1$ needs to be determined, offering simplicity. The calculation of the droplet oscillation frequency, $\omega$, is based on the following formula [21]:

$$\omega^2 = \frac{8 \cdot \sigma}{\rho_l \cdot r^3} - \frac{25 \cdot \mu_l^2}{4 \cdot \rho_l^2 \cdot r^4} \quad (4)$$

where, $\sigma$ is the fuel surface tension, $\rho_l$ is the fuel density, $\mu_l$ is the fuel dynamic viscosity and $r$ is the droplet radius. In the present study, all thermophysical properties involved in eq. (4) accommodate the temperature dependence as calculated by the HFO thermophysical properties model. It is worth mentioning that, in comparison to the TAB and ETAB models, the CAB model predicts higher ratios of child to parent droplet radius, in the entire Weber number range. This results in an improved representation of the fragmented liquid core, thus contributing to a more realistic prediction of the overall spray structure and the droplet size distribution [13].

*Collision model*

In the present HFO spray simulations, the standard collision model of the KIVA-3 code is utilized, in which only the coalescence and stretching (grazing collision) are taken into account. The collision model involves a sampling procedure for droplets of particles in the same computational cell [16].

*Evaporation model*

As the utilized model of marine HFO thermophysical properties considers marine HFO as an equivalent one-component heavy petroleum fraction of undefined composition, a single-component evaporation model accounting for the effect of fuel vapor superheating is utilized in the present study [16], [24].

*Ignition and combustion model*

The ignition model utilized in the present simulations of reactive HFO sprays is the simplified kinetic ignition model developed by Weisser et al. [25], in which the value of an ignition progress variable, governing the ignition delay through a transport conservation equation, serves as the ignition criterion. The ignition progress variable is a non-dimensional quantity, defined as the concentration of an intermediate species divided by a critical value. Modeling of the overall ignition delay is based on a detailed chemistry mechanism for n-heptane, utilizing a simplified system of characteristic times computed from Arrhenius type correlations. A computed value of the ignition progress variable greater than unity signals ignition for the corresponding computational cell, and activates the combustion model. In the present study, combustion modeling utilizes the characteristic time model of Kong et al. [26].

**Results and Discussion**

*Spray model calibration*

Calibration of the CAB spray model was performed for operating conditions corresponding to Case 1 and Case 5 (introduced in Table II), using the fine mesh (see Table I). Both cases are perceived as demanding, as they involve break-up, evaporation (Case 1) and combustion (Case 5), while they also correspond to conditions similar to those of marine engines. Spray propagation can be characterized by the evolution of the penetration of its tip as a function of time after the Start Of Injection (SOI) [27]. A good agreement between the computed and measured time history of penetration length, as well as ignition delay and location were used as the main criterion for calibrating the CAB spray model. It is noted that the value of exponent $n$ plays an important role, especially in reactive spray flow. In calibrating the spray model, the value of the initial spray angle, depending on the gas density, is prescribed based on experimental measurements [12]. The optimal constant values obtained are reported in Table V; these values were maintained for all other cases computed.

**Table V:** Optimal values of CAB model constants.

| Constant | Description | Value |
|---|---|---|
| $\theta$ | Initial spray angle [deg.] | 10 ~ 16 |
| $C_\lambda$ | jet break-up length | 5.5 |
| $k_1$ | time scale parameter for 'bag break-up' | 0.13 |
| $k_2$ | time scale parameter for 'stripping break-up' | calculated |
| $k_3$ | time scale parameter for 'catastrophic break-up' | calculated |
| $n$ | exponent in IDSD | 1.5 |

*Resolution tests*

Both spatial and temporal resolution tests were performed to check the dependence of computational results on discretization parameters. First, spatial resolution tests were performed, utilizing the three grids presented in Table I, for Case 1 (non-reactive evaporating spray). The maximum computational time step was in all cases $\Delta t=10^{-5}$ s. Figure 7 shows the calculated time history of spray penetration length for all three grids, which is compared with the corresponding experimental data of [12]. In general, there is very good agreement between the present CFD results and the experiment. For all grids, the results coincide in the initial stage of injection, and are very close to the experimental curve. Subsequently, there are small differences in the computed values of penetration length. As the very fine mesh (720,000 cells) is characterized by quite high computational cost, while giving results only slightly deviating from the fine mesh (260,000 cells), the latter is selected for the subsequent computational studies of HFO sprays. Finally, Case 1 was computed for different maximum time step values using the fine mesh. These temporal resolution tests involved maximum time step values ranging from $10^{-6}$ s to $10^{-4}$ s. Minimal variations in spray penetration length were observed for time steps lower than $10^{-5}$ s. Thus, a maximum time step of $\Delta t=10^{-5}$ s was selected for the subsequent computations. Figure 8 presents instantaneous snapshots of gas velocity and fuel vapor mass fraction at a time of 3 ms after SOI, at the horizontal plane including the injector. An increase of gas velocities in the fuel jet region is observed for increased resolution; this justifies the penetration length trends of Figure 7. The increase in penetration length tends to increase the spray area, and thus enhances the total evaporation rate; a corresponding trend is justified in the fuel vapor mass fraction iso-contours of Figure 8.

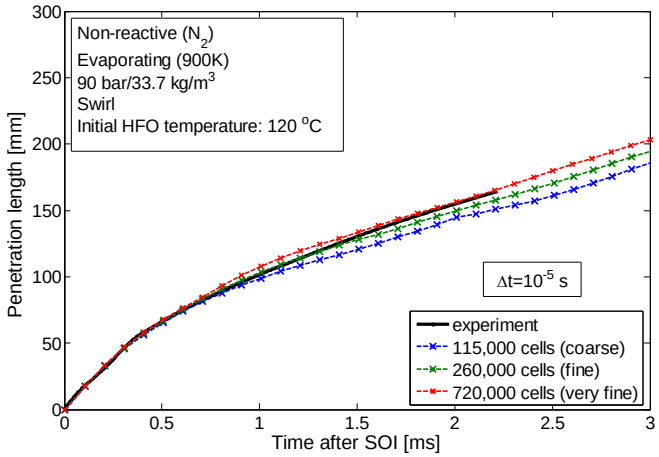


**Figure 7:** Case 1 (gas density of 33.7 kg/m$^3$): Calculated HFO penetration length versus time for three different computational grids, using the CAB model. The time step value is $10^{-5}$ s. The corresponding experimental curve of von Rotz et al. [12] is also included.

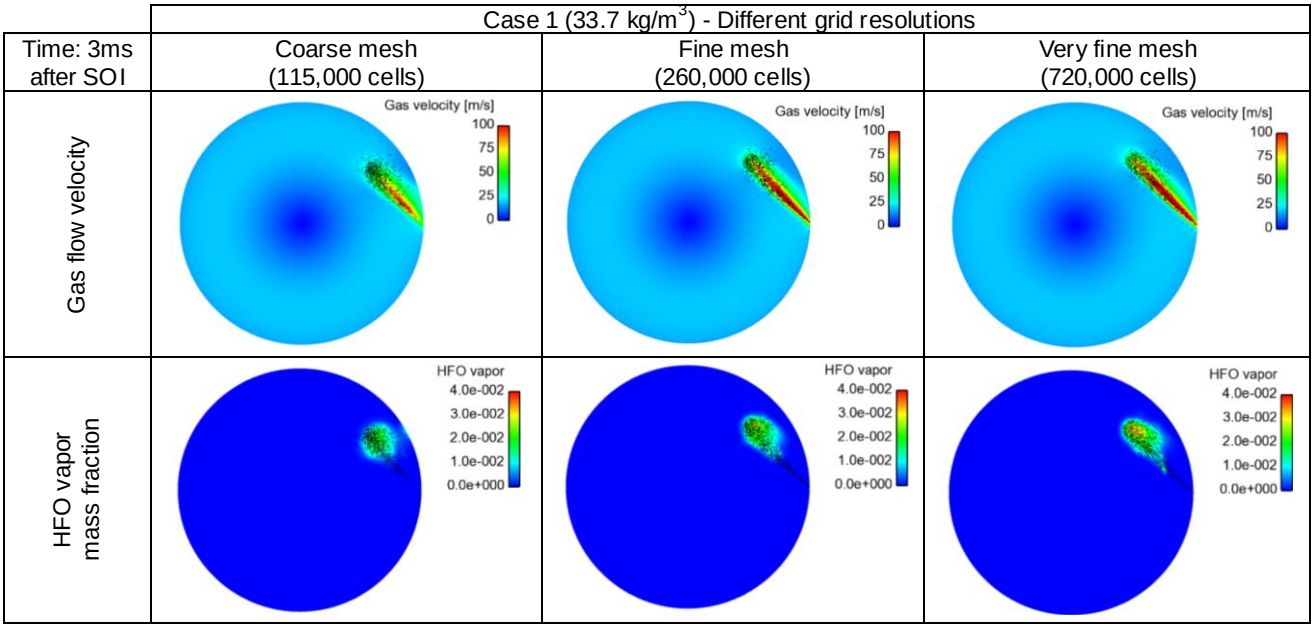


**Figure 8:** Case 1 (gas density of 33.7 kg/m$^3$): color-coded contours of gas velocity and HFO vapor mass fraction at the horizontal plane including the injector, 3.0 ms after SOI, for three computational grids.

*Non-reactive HFO spray studies*

The computed HFO penetration length versus time, for Case 1, Case 2 and Case 3, is presented in Figure 9; the experimental curves of [12] are also included. An overall very good agreement is observed. Further, Figure 10 presents snapshots of HFO vapor mass fraction, at the representative times of 1 ms and 3 ms after SOI, for Cases 1 and 3; here, the horizontal plane including the injector is considered. The results illustrate the strong impact of gas density on spray development, as the penetration length is significantly lower for the higher gas density. The trend is justified by the fact that the fuel spray experiences higher aerodynamic forces, resulting in higher values of Weber number. Also, no evaporation of HFO is observed in the initial stage of injection, while lower evaporation rates are subsequently observed for the high pressure case.

To further justify the low evaporation tendency of HFO, simulations are performed for relatively low ambient gas temperature, in particular 400 K, for the conditions corresponding to Case 4 (see Table II). Figure 11 presents snapshots of HFO vapor mass fraction in the SCC mid-plane, at 5 ms after SOI, while corresponding results for Case 1 (900 K, same gas density as Case 4) are also included. A zero value of evaporated HFO mass is verified for Case 4, even though the two spray jets are characterized by the same Weber number, and thus are expected to exhibit the same dynamics of spray break-up.

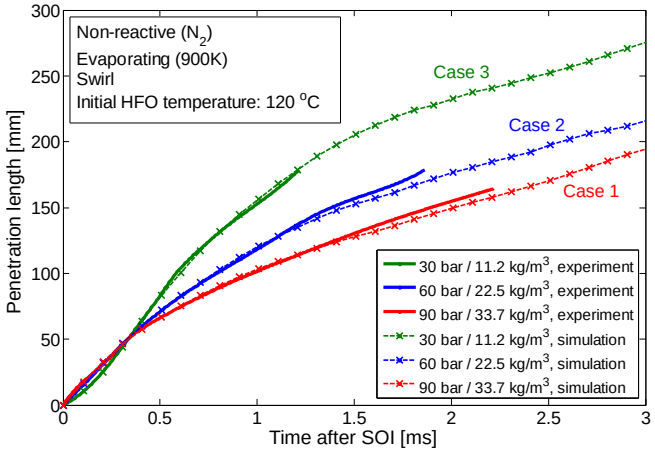


**Figure 9:** Computed time history of HFO penetration length, for Case 1, Case 2 and Case 3, corresponding to gas density of 33.7 kg/m$^3$, 22.5 kg/m$^3$ and 11.2 kg/m$^3$, respectively (non-reactive evaporating conditions). All Cases are characterized by swirling gas flow. The corresponding experimental curves of von Rotz et al. [12] are also included.

| | HFO vapor mass fraction | |
|---|---|---|
| Time after SOI | Case 1 (33.7 kg/m$^3$) | Case 3 (11.2 kg/m$^3$) |
| 1 ms | 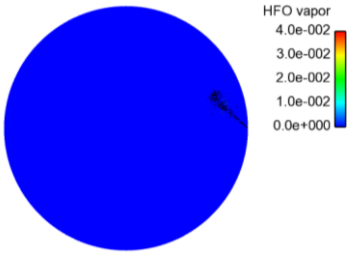 | 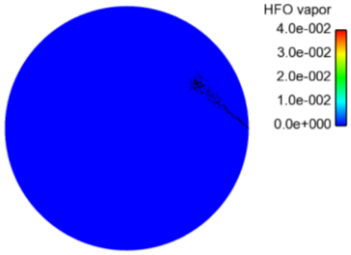 |
| 3 ms | 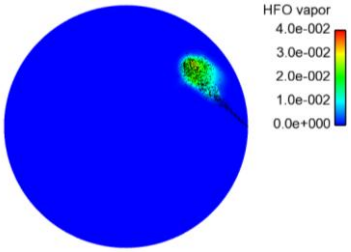 | 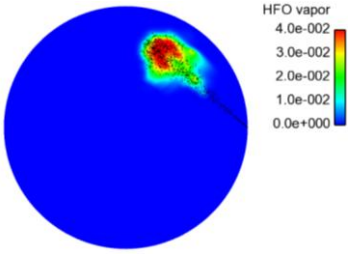 |



**Figure 10:** Cases 1 and 3 (non-reactive evaporating sprays): color-coded contours of HFO vapor mass fraction at the horizontal plane including the injector, at the representative time instants of 1 ms and 3 ms after SOI.

| | Non-reactive (33.7 kg/m$^3$) - HFO vapor mass fraction | |
|---|---|---|
| Time after SOI | Evaporating Case 1 (900K) | Non-evaporating Case 4 (400K) |
| 5 ms | 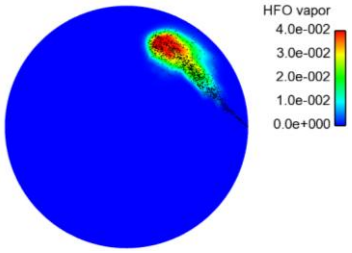 | 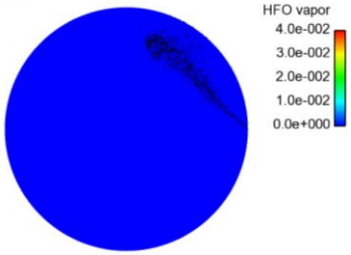 |



**Figure 11:** Color-coded contours of HFO vapor mass fraction at a plane including the injector, at 5.0 ms after SOI, for evaporating Case 1 (left) and non-evaporating Case 4 (right).

*Effect of HFO preheating*

In the present study, the impact of HFO preheating on spray propagation is also considered. To this end, the effect of injected fuel temperature under the conditions of Case 1 is investigated, by considering three temperature values, in particular 80 °C, 120 °C and 160 °C; the high end temperature range corresponds to representative values of kinematic viscosity of fuels used in large marine engines, i.e. 13 cSt. The computational results for penetration length versus time, for the evaporating Case 1, for different values of injected fuel temperature, are presented in Figure 12; the experimental results of [12], obtained for a fuel temperature of 120 °C, are also included. The computational results illustrate a marked difference between the spray development of "cold" (T=80 °C) and sufficiently heated fuel, with the "cold" spray characterized by substantially higher penetration, due to its minimal break-up. It is worth noting that, in all cases, the initial stage of linear development is similar for all temperatures. In the subsequent stage, spray development is found to be independent of preheating, for fuel temperatures higher than 120 °C. Figure 13 shows snapshots of the HFO vapor mass fraction distribution, at 3 ms after SOI, for Case 1, for different preheating temperatures, for the plane including the injector. An increase in evaporation rate with fuel preheating is observed, while minimal break-up is achieved for "cold" fuel. The conclusion for minimal cascade break-up of "cold" fuel is also confirmed in Figure 14, in which the spray structure is illustrated, including indications of Sauter Mean Diameter (SMD), at 3 ms after SOI. The results presented in this subsection demonstrate that the present modeling can properly account for the effects of HFO preheating on spray dynamics.

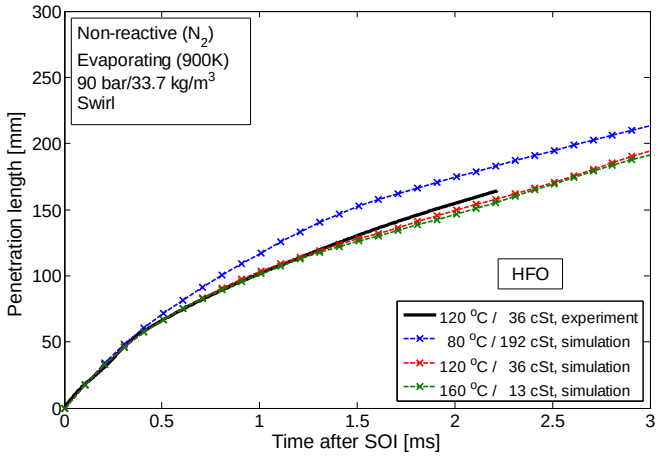


**Figure 12:** Case 1 (gas density of 33.7 kg/m$^3$): Computed HFO spray penetration length versus time, for different values of preheating temperature. The experimental results of von Rotz et al. [12], corresponding to an initial HFO temperature of 120 °C, are also included.

| | Case 1 (33.7 kg/m$^3$) - Different HFO preheating temperature | | |
|---|---|---|---|
| Time: 3ms after SOI | 80 °C | 120 °C | 160 °C |
| HFO vapor mass fraction | 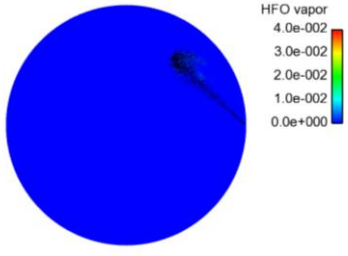 | 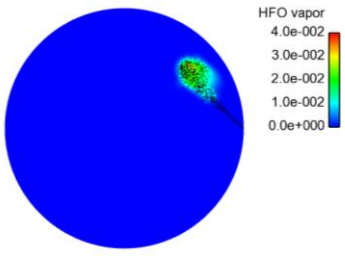 | 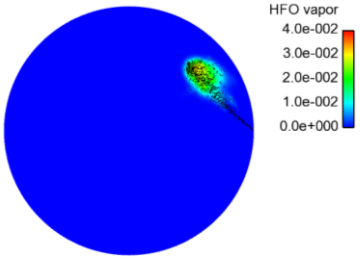 |



**Figure 13:** Case 1 (gas density of 33.7 kg/m$^3$): color-coded contours of HFO vapor mass fraction for initial fuel temperatures of 80 °C, 120 °C and 160 °C, at 3.0 ms after SOI, in a plane located at the height of the injector.

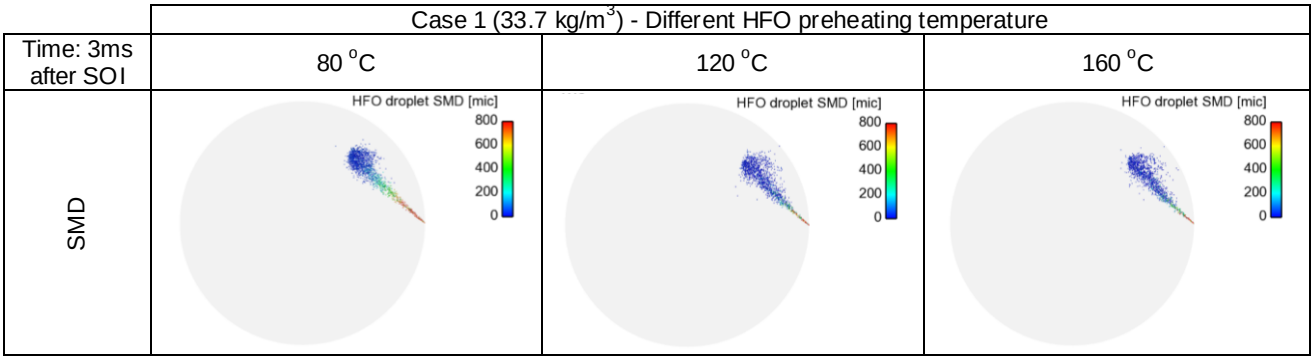


**Figure 14:** Case 1 (gas density of 33.7 kg/m$^3$): bottom view of spray structure and color-coded indications of SMD, for initial HFO temperatures of 80 °C, 120 °C and 160 °C, at 3.0 ms after SOI.

*Reactive HFO spray studies*

In the present work, first preliminary reactive spray CFD studies are performed and compared to corresponding experimental data, aiming at a characterization of reactive flow. The experiments have been conducted with HFO preheated to a temperature of about 120 °C and at a gas temperature of 915 °C (on average). The measured data have been subsequently processed appropriately in order to obtain average results for ignition delay and location. In the present simulations, the conditions of Case 5 are utilized (see Table II), which correspond to mean values of the gas pressure and temperature in the SCC. Further, the impact of HFO preheating is investigated again, by considering three values of initial HFO temperature, namely, 80 °C, 120 °C and 160 °C. The computational results in terms of ignition delay and location have been determined in a single computation, respectively, by averaging over all cells in which the non-dimensional ignition progress variable is greater than unity and an instantaneous burning rate is greater than zero. Figure 15 and Figure 16 present the computed ignition delay and location as a distance from the nozzle tip, respectively, for the reactive Case 5 and different injected fuel initial temperatures. The results of all series of experimental measurements are also included (corresponding to a preheating temperature of 120 °C), while the corresponding mean value is highlighted. A very good agreement between experiment and simulation is demonstrated. Also, the expected increase of ignition delay and distance between nozzle tip and ignition spot at decreasing values of fuel temperature is in general verified in the present computations. Further, Figure 17 presents an iso-surface characterized by a value of the ignition progress variable of 1.0, indicating the location of ignition, for the three values of fuel preheating temperature considered. The effect of swirl on ignition location is identified: the fuel vapor is convected by the swirling gas flow, which results in a displacement of the ignition point with respect to the spray centerline. Due to the more pronounced evaporation in the case of preheating to 160 °C, this displacement of fuel vapor also results in a longer absolute distance of the ignition point from the injector tip, in comparison to the case of preheating to 120 °C (see Figure 16).

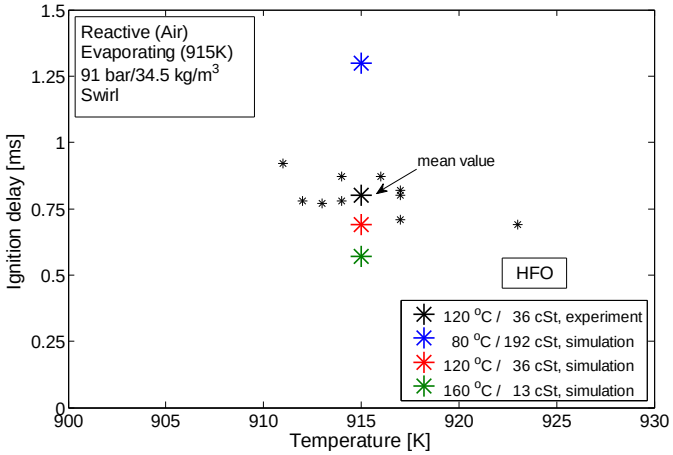


**Figure 15:** Case 5 (reactive spray): Computed and measured ignition delay times versus chamber air temperature. The computations correspond to an air temperature of 915 K, while three values of fuel preheating temperature are considered.

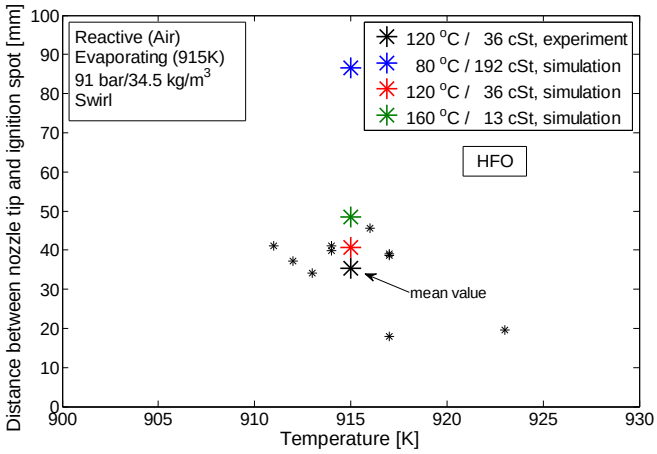


**Figure 16:** Case 5 (reactive spray): Computed and measured ignition location versus chamber air temperature. The computations correspond to an air temperature of 915 K, while three values of fuel preheating temperature are considered.

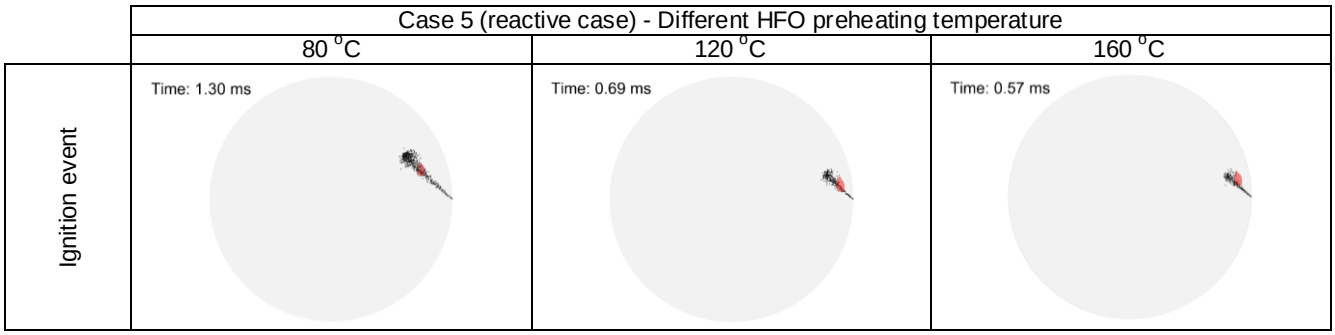


**Figure 17:** Case 5 (reactive spray): Bottom view of HFO spray structure at the ignition delay time, in which the iso-surface corresponding to a value of 1.0 for the ignition progress variable is included. Three values of fuel preheating temperature are considered.

Figure 18 presents computational results in terms of temperature iso-contours at the chamber mid-plane, for the reactive Case 5, at 20 ms after SOI, for the three values of fuel preheating temperature considered. The temperature distributions are indicative of flame lift-off, illustrating an increase of lift-off at decreasing initial HFO temperature.

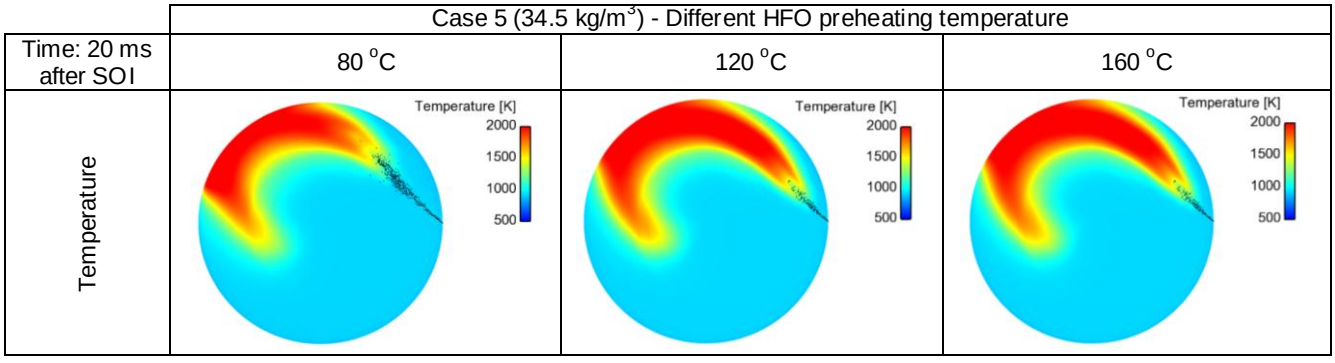


**Figure 18:** Case 5 (reactive spray): color-coded contours of temperature for initial fuel temperatures of 80 °C, 120 °C and 160 °C, at 20.0 ms after SOI, in a plane located at the height of the injector.

## Conclusions

In the present study, a thermophysical properties model recently developed by the authors has been applied to calculate the properties of the HFO utilized the SCC experiments of Wärtsilä Switzerland and ETH Zürich. The model has been further validated by deploying extensive CFD simulations of non-reactive and reactive sprays in the SCC, under conditions similar to those of large marine engines. To this end, a proper adaptation of the CAB spray model was achieved, accounting for the initial droplet size distribution, as well as for the number and size of droplets resulting from the secondary break-up.

For non-reactive sprays, computational results have demonstrated a very good agreement against experiments for the spray penetration length and overall spray development. The present computational results yield a proper representation of the fragmented liquid core near the nozzle tip, while also predicting the low evaporation tendency of HFO. Further, the effects of HFO preheating on the spray development, in particular penetration length, SMD distribution and evaporation rate, have been properly predicted by considering three representative temperature values. Minimal cascade break-up and evaporation rate, resulting in a longer penetration length, have been calculated for the lowest HFO preheating temperature (80 $^{o}$C).

First experimental results of reactive HFO sprays have been also reported, including ignition delay and location. CFD simulations accurately reproduce the experimentally identified HFO ignition characteristics, and also verify the strong effects of HFO preheating. Specifically, the ignition delay decreases for higher levels of initial HFO temperature, while the ignition location is strongly dependent on the intense swirling flow and evaporation rate.

The present development constitutes a strong basis for CFD studies of flow and combustion in large marine engines operating with HFO.

## Acknowledgements

The first author would like to thank the Norwegian Classification Society (DNV), for financing his doctoral thesis project. The experimental investigations have been conducted as part of the HERCULES-C project within EC's 7$^{th}$ Framework Program, Contract number SCP1-GA-2011-284354. Additional financial support by the Swiss Federal Government (SFOE Contract SI/500940-01, TP Nr 8100075, Project name "FlexiFuel Combustion") is gratefully acknowledged.

## References

[1] Eyring, V., Stevenson, D.S., Lauer, A., Dentener, F.J., Butler, T., Collins, W.J., Ellingsen, K., Gauss, M., Hauglustaine, D.A., Isaksen, I.S.A., Lawrence, M.G., Richter, A., Rodriguez, J.M., Sanderson, M., Strahan, S.E., Sudo, K., Szopa, S., van Noije, T.P.C., Wild, O., 2007, Atmospheric Chemistry and Physics, pp. 757-780.

[2] International Maritime Organization, http://www.imo.org

[3] MAERSK, "Slow steaming - the full story", http://www.maersk.com

[4] Wiesmann, A., February 2010, Wärtsilä technical journal, pp. 49-55.

[5] High-Efficiency R&D on Combustion with Ultra Low Emissions for Ships - HERCULES, http://www.hercules-c.org

[6] Kyrtatos, N.P., Hellberg, L., Poensgen, C., 2013, Paper No. 18, CIMAC Congress, Shanghai, China.

[7] Herrmann, K., Schulz, R., Weisser, G., 2007, Paper No. 98, CIMAC Congress, Vienna, Austria.

[8] Herrmann, K., Kyrtatos, A., Schulz, R., Weisser, G., von Rotz, B., Schneider, B., Boulouchos, K., 2009, Paper No 005, 11$^{th}$ Triennial International Annual Conference on Liquid Atomization and Spray Systems (ICLASS), Vail, Colorado USA.

[9] Pizza, G., Wright, Y.M., Weisser, G., Boulouchos, K., 2007, International Journal of Vehicle Design, Vol. 45, Nos. 1/2, pp. 80-99.

[10] de Hoog, P., Steernberg, K., Forget, S., 2010, Paper No. 70, CIMAC Congress, Bergen, Norway.

[11] Kontoulis, P., Kazangas, D., Kaiktsis, L., 2013, Paper No 63, 25$^{th}$ European Conference on Liquid Atomization and Spray Systems (ILASS), Chania, Greece.

[12] von Rotz, B., Herrmann, K., Weisser, G., Cattin, M., Bolla, M., Boulouchos, K., 2011, 24$^{th}$ European Conference on Liquid Atomization and Spray Systems (ILASS), Estoril, Portugal.

[13] Tanner, F.X., 2004, Atomization and Sprays, Vol. 14, pp. 211-242.

[14] Herrmann, K., von Rotz, B., Schulz, R., Weisser, G., Schneider, B. and Boulouchos, K., 2011, International Symposium on Marine Engineering (ISME), Kobe, Japan.

[15] Schmid, A., von Rotz, B., Bombach, R., Weisser, G., Herrmann, K. and Boulouchos, K., 2012, 8$^{th}$ International Conference on Modeling and Diagnostics for Advanced Engine Systems (COMODIA), Fukuoka, Japan.

[16] Amsden, A.A., O'Rourke, P.J., Butler, T.D., 1989, Los Alamos National Laboratories, LA-11560-MS.

[17] Amsden, A.A., 1993, Los Alamos National Laboratory, LA-12503-MS.

[18] American Petroleum Institute, 1997, "Technical data book, petroleum refining".
[19] Tanner, F.X., 1997, SAE 970050.
[20] Tanner, F.X., Weisser, G.A., 1998, SAE 980808.
[21] O'Rourke, P.J., Amsden, A.A., 1987, SAE 872089.
[22] Hiroyasu, H., Kadota, T., Arai, M., 1980, "Combustion Modeling in Reciprocating Engines", pp. 369-480.
[23] Liu, A.B., Reitz, R.D., 1993, Atomization and Sprays, Vol. 3, pp. 55-75.
[24] Baumgarten, C., 2006, "Mixture formation in internal combustion engines".
[25] Weisser G., Tanner F., Boulouchos K., 1998, SAE 981451.
[26] Kong, S.-C., Han, Z., Reitz, R.D., 1995, SAE 950278.
[27] Arcoumanis C., Gavaises M., French B., 1997, SAE 970799.